energies

MDPI

Article

Hydrodynamic Investigation of a Concentric Cylindrical OWC Wave Energy Converter

Yu Zhou [1,2], Chongwei Zhang [1,2] and Dezhi Ning [1,2,*]

[1] State Key Laboratory of Coastal and Offshore Engineering, Dalian University of Technology, Dalian 116024, China; yuzhouzhouyu@mail.dlut.edu.cn (Y.Z.); chongweizhang@dlut.edu.cn (C.Z.)
[2] Offshore Renewable Energy Research Center, Dalian University of Technology, Dalian 116024, China
* Correspondence: dzning@dlut.edu.cn

Received: 22 March 2018; Accepted: 16 April 2018; Published: 18 April 2018

Abstract: A fixed, concentric, cylindrical oscillating water column (OWC) wave energy converter (WEC) is proposed for shallow offshore sites. Compared with the existing shoreline OWC device, this wave energy device is not restricted by the wave directions and coastline geography conditions. Analytical solutions are derived based on the linear potential-flow theory and eigen-function expansion technique to investigate hydrodynamic properties of the device. Three typical free-surface oscillation modes in the chamber are discussed, of which the piston-type mode makes the main contribution to the energy conversion. The effects of the geometrical parameters on the hydrodynamic properties are further investigated. The resonance frequency of the chamber, the power extraction efficiency, and the effective frequency bandwidth of the device is discussed, amongst other topics. It is found that the proposed OWC-WEC device with a lower draft and wider chamber breadth has better power extraction ability.

Keywords: oscillating water column; wave energy; wave diffraction; eigen-function expansion; potential flow theory; air chamber

1. Introduction

Sustainable energy from ocean waves has drawn people's attention for over 40 years. So far, there have been a large number of wave energy converters proposed [1,2]. The energy extraction from waves mainly relies on the hinged mechanical motions [3], individual body oscillations [4], water overtopping to reservoirs [5], or trapped air pockets in oscillating water column (OWC) chambers [6]. Compared with those mechanical oscillators, the OWC wave energy converter has no moving parts in the water, which is an attractive feature in terms of survivability and maintenance convenience [7].

Up to now, the OWCs have been the most widely used wave energy converters in practice. The first OWC device deployed into the sea on a large scale was in Japan [8]. After that, a number of OWC devices have been proposed and deployed. For example, a breakwater equipped with OWC plant was finished with a 40 kW Wells turbine in the Sea of Japan [9]. A small shoreline OWC (75 kW) was built for academic studying at the island of Islay in Scotland. In Guangdong Province of China, a shore-fixed OWC device (100 kW) was completed in 2001 [10]. Recently, a new U-type OWC has been being installed in breakwaters, which is expected to show dramatically improved absorption width for fixed installations [11]. However, OWCs inserted in breakwaters can be installed in zones with low available energy [12]. It should be noticed that the above-mentioned OWC-WECs are often based on shoreline or near-shore regions, which not only have the potential to harm the coastline environment but also are limited in terms of the deployment scale. To reduce the environmental impact and increase the scale of deployment, the wave energy exploitation tends to progress to offshore sites [13]. Typical examples are the 110 kW Mighty Whale [14] and the OE Buoy in Galway Bay [15].

In this study, a concentric cylindrical OWC-WEC is innovatively designed for offshore sites with multiple wave directions. From economic and risk considerations, a fixed OWC structure is preferred. As shown in Figure 1, the structure can be considered as an upside-down cylindrical bucket supported by a cylinder. A concentric cylindrical chamber is formed. A beam is used to connect the chamber and the cylinder as shown in Figure 1b. The energy is transformed from the wave to the air by an oscillating water column moving up and down in the chamber. As the bidirectional airflow flows through the orifice on the top of the chamber, the turbine is driven to be an electricity generator. Compared with the shoreline OWC devices that can only capture the wave energy from one direction, the application of the present-type wave energy device is not restricted by the wave direction and coastline geography condition.

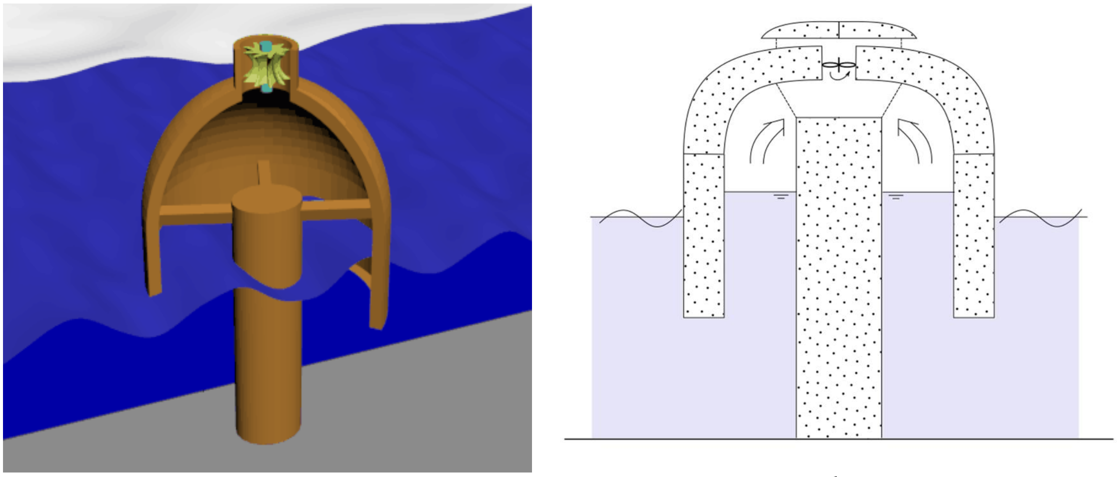

(**a**) (**b**)

Figure 1. Concept of the concentric cylindrical OWC-WEC, (**a**) 3D effect picture; (**b**) the profile of the chamber.

At the preliminary study stage, the efficiency and hydrodynamic properties of the structure must be identified before the optimized dimension parameters can be given. The analytic method has been used for the preliminary research of the OWC-WECs efficiently by scholars. For example, Garrett [16] derived the linear diffraction solution of a fistulous suspended cylinder in shallow water. Sarmento and Falcão [17] derived a two dimensional analytical model to investigate the effects of linear and nonlinear power take-off system on hydrodynamic properties of OWC-WEC. Zhu and Mitchell [18] presented a diffraction analytical solution of waves around a fistulous cylinder without thickness. Martin-Rivas and Mei [19] presented a linear theory of an OWC which is installed on a straight coast for studying the effects of the coastline on wave power conversion. Martin-Rivas and Mei [20] simulated a thin cylindrical OWC-WEC, which was installed in a breakwater. It is concluded that air compressibility can broaden the effective bandwidth of extraction efficiency with the specific chamber volume. Konispoliatis [21] developed an analytical model to study the hydrodynamics of an OWC-WECs array. Three-unit arrays are discussed, which can be used as a floating wind-turbine foundation. In the present study, an analytical solution based on linear potential-flow theory is derived for the present OWC-WEC.

The present paper is organized as follows. Section 2 describes the power take-off model and analytical solutions of the hydrodynamic problem. In Section 3, the accuracy and convergence of the analytical model are validated. Then, effects of environmental and geometrical parameters on the resonant wave modes and hydrodynamic properties are studied systematically. Conclusions are summarized in Section 4.

2. Mathematical Problem

The proposed OWC-WEC structure is fixed and rigid in the sea. The submerged part can be considered as a concentric cylindrical geometry as in Figure 2. In this study, the draft of the chamber is d. The water depth is h. The bottom-mounted cylinder and the internal and external surfaces of the chamber have the radius R_1, R_2, and R_3, respectively. A Cartesian coordinate system O-xyz is defined with the origin O on the undisturbed free surface, z-axis pointing vertically upwards, and x-axis coinciding with the direction of incident waves. The structure is axisymmetric about the Oz axis.

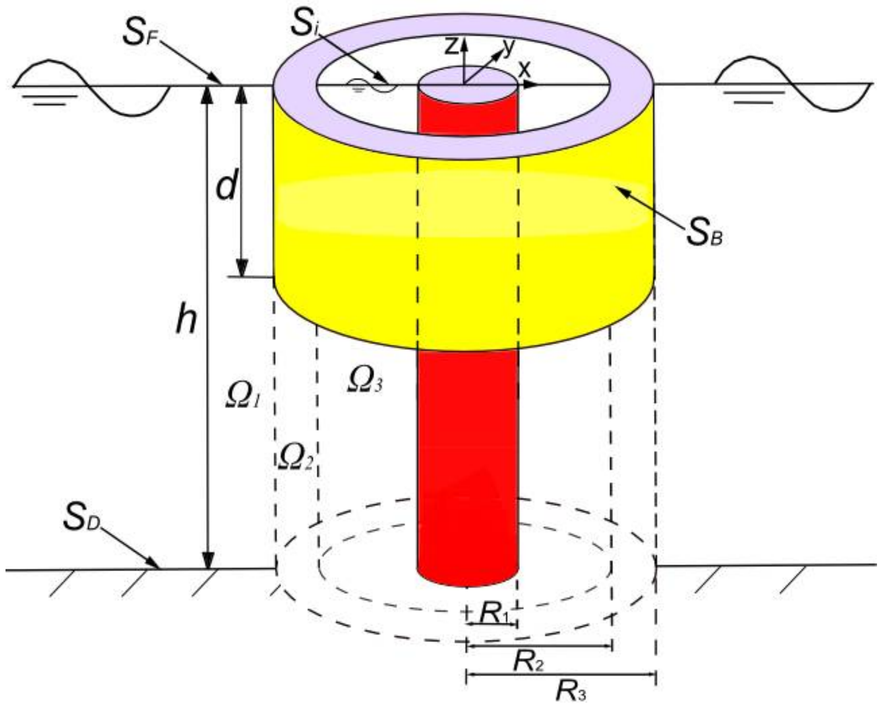

Figure 2. Schematic of the proposed OWC-WEC foundation.

2.1. Power Take-Off Model

In present study, the air in the chamber of the OWC-WEC is considered to be compressible and motion-isentropic. Additionally, all time-dependent variables in the problem are assumed to be harmonic. Then, the time-independent air pressure is introduced:

$$P_a = \mathrm{Re}[P_0 e^{-i\omega t}] \tag{1}$$

in which ω is the wave angular frequency, t is the time, Re is the real part of a complex variable, P_0 is the complex amplitude of the pressure, and $i = \sqrt{-1}$. A Wells turbine, which is installed at the top of the air chamber, is forced to rotate by oscillating air flow. The mass flux rate of the air across the Wells turbine is proportional to the air pressure in the chamber [17,22], and the relationship between the air mass flux and the turbine characteristics can be expressed as [18]

$$q_0 = \left(\frac{KD}{N\rho_a} - \frac{i\omega V_0}{c^2 \rho_a} \right) P_0 \tag{2}$$

in which q_0 is the amplitude of the air volume flux, V_0 is the mean chamber volume, ρ_a is the air density, N is the turbine rotational speed in r.p.m., D is diameter of the turbine rotor, c is the sound velocity in air, and K is an empirical coefficient depending on the design of the turbines.

Based on the linear theory, the volume flux in the chamber is the sum of volume fluxes due to wave radiation and diffraction. The wave radiation occurs in the situation when the wave motion is purely caused by the oscillating air pressure of the chamber. The wave diffraction is due to scattering of incident waves when the air pressures inside and outside the chamber are identical. Thus, complex amplitude of the volume flux has two components

$$q_0 = q_D + P_0 q_R \tag{3}$$

in which q_R and q_D are connected with the radiation and diffraction problems, respectively. For a radiation problem, an added mass coefficient $\widetilde{C}$ and a damping coefficient $\widetilde{B}$ can be obtained [23]. Complex amplitude of the volume flux q_R, which is caused by the unit air pressure, can be expressed as

$$q_R = \left(-\widetilde{B} + i\widetilde{C}\right) \tag{4}$$

By substituting Equations (3) and (4) into Equation (2), the air pressure in the chamber can be expressed as follows

$$P_0 = \frac{q_D}{\left[\left(\frac{KD}{N\rho_a} + \widetilde{B}\right) - i\left(\widetilde{C} + \frac{\omega V_0}{c^2 \rho_a}\right)\right]} \tag{5}$$

in which q_D is solved from the wave diffraction problem, and $\widetilde{B}$ and $\widetilde{C}$ can be obtained by solving the radiation problem with unit forced pressure.

The time-averaged value of the power captured by the turbine is [18]

$$P_{out} = \frac{KD}{2N\rho_a}|P_0|^2 \tag{6}$$

The power extraction efficiency ξ can be calculated as [18]

$$\xi = \frac{kP_{out}}{\rho g A C_g/2} = \frac{gkR_2}{\omega C_g}\frac{\chi|Q_D|^2}{(\chi+B)^2+(\beta+C)^2} \tag{7}$$

in which $Q_D = \omega q_D/(AR_2 g)$, $(B, C) = \left(\omega\rho\widetilde{B}, \omega\rho\widetilde{C}\right)/R_2$, $\chi = \rho KD\omega/(N\rho_a R_2)$, $\beta = V_0\omega^2\rho/\left(c_a^2 R_2 \rho_a\right)$ are nondimensional parameters. χ characterizes the turbine, β represents the air compressibility. C_g is the group velocity of the incident wave, g is the gravitational acceleration, ρ denotes the water density, and k is the incident wave number.

2.2. Solution of Boundary Value Problem

Under the assumption that the fluid is incompressible, inviscid, and flow-irrotational, the proposed problem is considered. The complex velocity potential $\varphi(x, y, z, t)$ around the structure is introduced to describe the properties of the fluid. For small amplitude wave, the potential φ satisfies the following linearized boundary value problem

$$\nabla^2\varphi = 0, \text{in } \Omega \tag{8}$$

$$\frac{\partial\varphi}{\partial n} = 0, S_B \textit{ and } S_D \tag{9}$$

$$\frac{\partial\varphi}{\partial t} + g\frac{\partial\varphi}{\partial z} = \begin{cases} -\sigma_R P/\rho, & \text{on} \quad S_i \\ 0, & \text{on} \quad S_F \end{cases} \tag{10}$$

in which Ω, S_D, S_i, S_F, and S_B represent the mean fluid domain, water bottom, internal free surface, external free surface, and wet body surface, respectively. The operator $\partial/\partial n$ denotes the normal derivative of a variable on the impenetrable solid surface. For completeness, a radiation condition is also required on the open boundary. For the time-harmonic, velocity potential with angular frequency ω can be expressed as

$$\varphi(x, y, z, t) = \mathrm{Re}\left[\phi(x, y, z)e^{-i\omega t}\right] \tag{11}$$

in which ϕ is a spatial function. It should be highlighted that σ_R is used as a switch between the radiation and diffraction problem. For the radiation problem, $\sigma_R = 1$ is set and the pressure amplitude in chamber is $P_0 = 1$ in Equation (1). For the diffraction problem, $\sigma_R = 0$ is set.

Based on the axisymmetric geometry of the OWC-WEC, the radiation and diffraction problem can be solved in the cylindrical polar coordinates (r, θ, z) with

$$x = r\cos\theta \text{ and } y = r\sin\theta \tag{12}$$

The fluid domain can be divided into three subdomains, as shown in Figure 2. The external subdomain is Ω_1 with $r \geq R_3$ and $-h \leq z \leq 0$, the lower subdomain Ω_2 with $R_2 \leq r \leq R_3$ and $-h \leq z \leq -d$, and the internal subdomain Ω_3 with $R_1 \leq r \leq R_2$ and $-h \leq z \leq 0$. Correspondingly, the potentials in Ω_1, Ω_2, and Ω_3 are expressed by $\phi^{(1)}$, $\phi^{(2)}$, and $\phi^{(3)}$, respectively.

The boundary value problem with respect to $\phi^{(1)}$ can be founded as follows

$$\nabla^2\phi^{(1)} = 0, \text{in } \Omega_1 \tag{13}$$

$$\frac{\partial\phi^{(1)}}{\partial z} = 0 \text{ for } r \geq R_3 \text{ and } z = -h \tag{14}$$

$$\frac{\partial\phi^{(1)}}{\partial z} = \frac{\omega^2}{g}\phi^{(1)}, \text{ for } r \geq R_3 \text{ and } z = 0 \tag{15}$$

$$\begin{cases} \phi^{(1)} = \phi^{(2)} \\ \partial\phi^{(1)}/\partial r = \partial\phi^{(2)}/\partial r \end{cases}, \text{ for } r = R_3 \text{ and } -h \leq z \leq -d \tag{16}$$

$$\partial\phi^{(1)}/\partial r = 0, \text{ for } r = R_3 \text{ and } -d \leq z \leq 0 \tag{17}$$

The radiation condition is also needed for $r \to \infty$.

For $\phi^{(2)}$, the boundary value problem corresponds to the following

$$\nabla^2\phi^{(2)} = 0, \text{ in } \Omega_2 \tag{18}$$

$$\frac{\partial\phi^{(2)}}{\partial z} = 0, \text{ for } R_2 \leq r \leq R_3 \text{ and } z = -d \tag{19}$$

$$\frac{\partial\phi^{(2)}}{\partial z} = 0, \text{ for } R_2 \leq r \leq R_3 \text{ and } z = -h \tag{20}$$

$$\begin{cases} \phi^{(2)} = \phi^{(1)} \\ \partial\phi^{(2)}/\partial r = \partial\phi^{(1)}/\partial r \end{cases}, \text{ for } r = R_3 \text{ and } -h \leq z \leq -d \tag{21}$$

$$\begin{cases} \phi^{(2)} = \phi^{(3)} \\ \partial\phi^{(2)}/\partial r = \partial\phi^{(3)}/\partial r \end{cases}, \text{ for } r = R_2, \text{ and } -h \leq z \leq -d \tag{22}$$

The $\phi^{(3)}$ could be obtained from the following boundary value problem

$$\nabla^2\phi^{(3)} = 0, \text{ in } \Omega_2 \tag{23}$$

$$\frac{\partial\phi^{(3)}}{\partial z} = 0, \text{ for } R_1 \leq r \leq R_2 \text{ and } z = -h \tag{24}$$

$$\frac{\partial \phi^{(3)}}{\partial z} - \frac{\omega^2}{g}\phi^{(3)} = \frac{i\omega\sigma_R P_0}{\rho g}, \text{ for } R_1 \leq r \leq R2, \text{ at } z = 0 \tag{25}$$

$$\left\{ \begin{array}{c} \phi^{(3)} = \phi^{(2)} \\ \partial\phi^{(3)}/\partial r = \partial\phi^{(2)}/\partial r \end{array} \right., \text{ for } r = R_2, \text{ and } -h \leq z \leq 0 \tag{26}$$

$$\partial\phi^{(3)}/\partial r = 0, \text{ for } r = R_2, \text{ and } -d \leq z \leq 0 \tag{27}$$

$$\partial\phi^{(3)}/\partial r = 0, \text{ for } r = R_1, \text{ and } -h \leq z \leq 0 \tag{28}$$

In Ω_3, P_0 is constant, and then the linear transformation can be made

$$\phi^{(3)} = \phi^* - i\sigma_R P_0/\rho\omega \tag{29}$$

in which ϕ^* satisfies the original system (23)–(28) in Ω_3, and then the inhomogeneous free surface condition (25) can be rewritten as

$$\frac{\partial \phi^*}{\partial z} = \frac{\omega^2}{g}\phi^*, \text{ for } R_1 \leq r \leq R_2 \text{ and } z = 0 \tag{30}$$

2.3. Mathematical Solution

In cylindrical polar coordinate system, the Laplace's equation of ϕ could be written as

$$\nabla^2\phi(r,\theta,z) = \frac{1}{r^2}\frac{\partial^2\phi}{\partial\theta^2} + \frac{1}{r}\frac{\partial}{\partial r}\left(r\frac{\partial\phi}{\partial r}\right) + \frac{\partial^2\phi}{\partial z^2} = 0 \tag{31}$$

Based on the method of separation of variables, ϕ may be assumed to be $\phi(r,\theta,z) = R(r)\Theta(\theta)Z(z)$. Then, Equation (31) can be rewritten by three ordinary differential equations as

$$\frac{d^2Z}{dz^2} + \alpha^2 Z = 0 \tag{32}$$

$$\frac{d^2\Theta}{d\theta^2} + \beta^2\Theta = 0 \tag{33}$$

$$r\frac{d}{dr}\left(r\frac{dR}{dr}\right) - \left(\alpha^2 r^2 + \beta^2\right)R = 0 \tag{34}$$

Both α^2 and β^2 are constants here.

In subdomain Ω_1, the solution of Equation (32) has the form:

$$Z(z) = \sum_{n=0}^{\infty} B_n Z_n^{(I)} \tag{35}$$

in which B_n denote constant coefficients and $Z_n^{(I)}$ are vertical eigen-functions. Further, taking the boundary conditions (i.e., Equations (14), (15), (19), (20), (24) and (30)) into account leads to the expression $Z_n^{(I)}$ for each subdomain as

$$Z_n^{(1)}(z) = Z_n^{(3)}(z) = \left\{ \begin{array}{c} \cosh k(z+h),\ n = 0 \\ \cos k_n(z+h), n \geq 1 \end{array} \right. \tag{36}$$

$$Z_n^{(2)}(z) = \begin{cases} 1, & n = 0 \\ \cos k_n^{(2)}(z+h), & n \geq 1 \end{cases} \tag{37}$$

in which $\{k_n; n = 1, 2, \cdots\}$ and k are positive real roots of the dispersion equations

$$\omega^2/g - k\tanh kh = 0 \tag{38}$$

$$\omega^2/g + k_n \tan k_n h = 0 \tag{39}$$

and $\left\{k_n^{(2)}; n = 1, 2, \cdots\right\}$ can be obtained from

$$k_n^{(2)} = n\pi/(h-d) \tag{40}$$

In each subdomain, the set of vertical eigen-functions is complete and satisfies the orthogonality relations as

$$\int_{-h}^{0} Z_m^{(1)} Z_n^{(1)} dz = 0, \text{ and } \int_{-h}^{-d} Z_m^{(2)} Z_n^{(2)} dz = 0 \text{ for } m \neq n \tag{41}$$

For Θ, with the continuity condition (i.e., $\Theta(\theta) = \Theta(\theta + 2\pi)$), the solution of Equation (33) can be written as

$$\Theta(\theta) = \sum_{m=0}^{\infty} B_m \Theta_m \tag{42}$$

in which B_m denote constant coefficients and Θ_m are circumferential eigen-functions as

$$\Theta_m(\theta) = \cos(m\theta), m = 0, 1, 2, \cdots \tag{43}$$

Equation (34) is the modified Bessel's equation

$$r\frac{d}{dr}\left(r\frac{dR}{dr}\right) - \left(k_n^2 r^2 + m^2\right) R = 0, \text{ for } m, n = 0, 1, 2, \cdots \tag{44}$$

with $k_0 = -ik$. The solution can be expressed as

$$R^{(I)}(r) = \sum_{m=0}^{\infty} \sum_{n=0}^{\infty} R_{mn}^{(I)}, \text{ for } m, n = 0, 1, 2, \cdots \tag{45}$$

In Ω_1, the potential of the incident wave can be written as

$$\phi_I(r, \theta, z) = \underbrace{\left(-\frac{igA}{\omega \cosh kh}\right)}_{E} \left[e^{ikr\cos\theta}\right] Z_0^{(1)}(z) = E\left[\sum_{m=0}^{\infty} \varepsilon_m i^m J_m(kr)\cos(m\theta)\right] Z_0^{(1)}(z) \tag{46}$$

in which A is the wave amplitude, $\varepsilon_m = \{1, \text{ for } m = 0;\ 2, \text{ for } m \geq 1\}$ is the Neumann symbol, and J_m is the first-kind of Bessel function of order m. The radiation condition is also satisfied to guarantee that the radiated waves propagate away from the structure. Then, the R_{mn} term can be written as

$$R_{mn}^{(1)}(r) = \begin{cases} B_{mn} H_m^{(1)}(kr), n = 0 \\ B_{mn} K_m(k_n r), n \geq 1 \end{cases}, \text{ for } m = 0, 1, 2, \cdots \tag{47}$$

in which B_{mn} is a constant coefficient, and $H_m^{(1)}$ and K_m are the first-kind of Hankel function and the second-kind of modified Bessel function, respectively, both of order m.

In Ω_2, $R_{mn}^{(2)}$ has the following expression

$$R_{mn}^{(2)} = \begin{cases} C_{00} + D_{00} \ln r, m = 0, n = 0 \\ C_{m0} r^m + D_{m0} r^{-m}, m \neq 0, n = 0 \\ C_{mn} I_m\left(k_n^{(2)} r\right) + D_{mn} K_m\left(k_n^{(2)} r\right), n \geq 1 \end{cases} \tag{48}$$

in which C_{mn}, D_{mn} also denote constant coefficients, and I_m is the first-kind of modified Bessel functions of order m. Note that the following relationship is satisfied for the case of $n = 0$

$$I_m(k_0r) = (-1)^m J_m(kr) \text{ and } K_m(k_0r) = \frac{\pi}{2} i^{m+1} H_m^{(1)}(kr) \tag{49}$$

In Ω_3, it has

$$R_{mn}^{(3)} = \begin{cases} A_{mn}J_m(kr) + E_{mn}Y_m(kr), n = 0 \\ A_{mn}I_m(k_nr) + E_{mn}K_m(k_nr), n \geq 1 \end{cases} \tag{50}$$

in which A_{mn}, E_{mn} are constant coefficients, and Y_m is the second kind of Bessel functions of order m. Further, with the boundary condition at $r = R_1$, the following relationship is further satisfied

$$A_{mn} = S_{mn}E_{mn} \text{ with } S_{mn} = \begin{cases} -\frac{dJ_m(ka)}{dr} / \frac{dY_m(ka)}{dr}, n = 0 \\ -\frac{dI_m(k_na)}{dr} / \frac{dK_m(k_na)}{dr}, n \geq 1 \end{cases} \tag{51}$$

Then, the general solution of ϕ in each subdomain can be expressed as

$$\begin{aligned} \phi^{(1)}(r,\theta,z) &= \sigma_D E \sum_{m=0}^{\infty} \varepsilon_m i^m \cos(m\theta) J_m(kr) Z_0^{(1)}(z) \\ &+ E \sum_{m=0}^{\infty} \varepsilon_m i^m \cos(m\theta) \left[\sum_{n=0}^{\infty} B_{mn} P_{mn}^{(1)}(r) Z_n^{(1)}(z) \right] \end{aligned} \tag{52}$$

$$\phi^{(2)}(r,\theta,z) = \sum_{m=0}^{\infty} \cos(m\theta) \sum_{n=0}^{\infty} \left[C_{mn}P_{mn}^{(2)}(r) + D_{mn}Q_{mn}^{(2)}(r) \right] Z_n^{(2)}(z) \tag{53}$$

$$\phi^{(3)}(r,\theta,z) = \sum_{m=0}^{\infty} \cos(m\theta) \sum_{n=0}^{\infty} \left[A_{mn}P_{mn}^{(3)}(r) Z_n^{(3)}(z) \right] - \frac{i\sigma_R P_0}{\rho\omega} \tag{54}$$

with

$$P_{mn}^{(1)}(r) = \left\{ H_m^{(1)}(kr), n = 0; K_m(k_nr), n \geq 1 \right\} \tag{55}$$

$$P_{mn}^{(2)}(r) = \left\{ 1, m = 0, n = 0; r^m, m \neq 0, n = 0; I_m\left(k_n^{(2)}r\right), n \geq 1 \right\} \tag{56}$$

$$Q_{mn}^{(2)}(r) = \left\{ \ln r, m = 0, n = 0; r^{-m}, m \neq 0, n = 0; K_m\left(k_n^{(2)}r\right), n \geq 1 \right\} \tag{57}$$

$$P_{mn}^{(3)}(r) = \begin{cases} J_m(kr) + S_{mn}H_m^{(1)}(kr), n = 0 \\ I_m(k_nr) + S_{mn}K_m(k_nr), n \geq 1 \end{cases} \tag{58}$$

Equations (52)–(54) have to satisfy the boundary conditions at $r = R_2$ and $r = R_3$. Additionally, $\sigma_D = 1 - \sigma_R$ is a switch to the diffraction problem. In order to take advantage of the orthogonality relations, the boundary conditions can be rewritten as

$$\int_{-h}^{-d} \phi^{(1)}(R_3,\theta,z) Z_n^{(2)}(z) dz = \int_{-h}^{-d} \phi^{(2)}(R_3,\theta,z) Z_n^{(2)}(z) dz \tag{59}$$

$$\int_{-h}^{-d} \phi^{(3)}(R_2,\theta,z) Z_n^{(2)}(z) dz = \int_{-h}^{-d} \phi^{(2)}(R_2,\theta,z) Z_n^{(2)}(z) dz \tag{60}$$

$$\int_{-h}^{0} \frac{d\phi^{(1)}(R_3,\theta,z)}{dr} Z_n^{(1)}(z) dz = \int_{-h}^{-d} \frac{d\phi^{(2)}(R_3,\theta,z)}{dr} Z_n^{(1)}(z) dz \tag{61}$$

$$\int_{-h}^{0} \frac{d\phi^{(3)}(R_2,\theta,z)}{dr} Z_n^{(3)}(z) dz = \int_{-h}^{-d} \frac{d\phi^{(2)}(R_2,\theta,z)}{dr} Z_n^{(3)}(z) dz \tag{62}$$

By substituting the general solutions of ϕ into these conditions and truncating each infinite series to M terms, it can lead to the following linear system of equations

$$\begin{aligned}\sum_{n=0}^{M} B_{mn}\left[E\varepsilon_m i^m P_{mn}^{(1)}(R_3)a_{nl}\right] - \sum_{n=0}^{M} C_{mn}\left[P_{mn}^{(2)}(R_3)b_{nl}\right] - \sum_{n=0}^{M} D_{mn}\left[Q_{mn}^{(2)}(R_3)b_{nl}\right] \\ = \left[-\sigma_D E\varepsilon_m i^m J_m(kR_3)a_{0l}\right]\end{aligned} \tag{63}$$

$$\sum_{n=0}^{M} A_{mn}\left[P_{mn}^{(3)}(R_2)a_{nl}\right] - \sum_{n=0}^{M} C_{mn}\left[P_{mn}^{(2)}(R_2)b_{nl}\right] - \sum_{n=0}^{M} D_{mn}\left[Q_{mn}^{(2)}(R_2)b_{nl}\right] = e_{0l} \tag{64}$$

$$\begin{aligned}\sum_{n=0}^{M} B_{mn}\left[E\varepsilon_m i^m \frac{dP_{mn}^{(1)}(R_3)}{dr}d_{nl}\right] - \sum_{n=0}^{M} C_{mn}\left[\frac{dP_{mn}^{(2)}(R_3)}{dr}c_{nl}\right] - \sum_{n=0}^{M} D_{mn}\left[\frac{dQ_{mn}^{(2)}(R_3)}{dr}c_{nl}\right] \\ = -E\varepsilon_m i^m k\frac{dJ_m(kR_3)}{dr}d_{0l}\end{aligned} \tag{65}$$

$$\sum_{n=0}^{M} A_{mn}\left[\frac{dP_{mn}^{(3)}(R_2)}{dr}d_{nl}\right] - \sum_{n=0}^{M} C_{mn}\left[\frac{dP_{mn}^{(2)}(R_2)}{dr}c_{nl}\right] - \sum_{n=0}^{M} D_{mn}\left[\frac{dQ_{mn}^{(2)}(R_2)}{dr}c_{nl}\right] = 0 \tag{66}$$

with

$$\begin{aligned} a_{nl} = \int_{-h}^{-d} Z_n^{(3)} Z_l^{(2)} dz = \int_{-h}^{-d} Z_n^{(1)} Z_l^{(2)} dz; b_{nl} = \int_{-h}^{-d} Z_n^{(1)} Z_l^{(1)} dz = \int_{-h}^{-d} Z_n^{(3)} Z_l^{(3)} dz; \\ c_{nl} = \int_{-h}^{-d} Z_n^{(2)} Z_l^{(3)} dz = \int_{-h}^{-d} Z_n^{(2)} Z_l^{(1)} dz; d_{nl} = \int_{-h}^{0} Z_n^{(3)} Z_l^{(3)} dz = \int_{-h}^{0} Z_n^{(1)} Z_l^{(1)} dz; \\ e_{0l} = \int_{-h}^{-d} i\sigma_R P_0/\rho\omega Z_l^{(2)} dz; \end{aligned} \tag{67}$$

By letting $m = 0 \sim M$, $l = 0 \sim M$, and $n = 0 \sim M$ in the eigen-function expansions terms, (M + 1) systems of equations can be obtained. For a specific m, the linear equations could be assembled as

$$[G(m)]_{[4\times(M+1)]\times[4\times(M+1)]}\mathbf{X} = \mathbf{T}, \tag{68}$$

with

$$\mathbf{X} = [A_{mn}, B_{mn}, C_{mn}, D_{mn}]^T \text{ for } n = 0, 1, \ldots, M \tag{69}$$

Once the coefficients A_{mn}, B_{mn}, C_{mn}, and D_{mn} are known, the velocity potential in each domain can be obtained based on Equations (52)–(54). The complex amplitude of volume flux can be calculated by the free-surface integration

$$q_D = \iint_{S_i} \frac{\partial\phi_3}{\partial z} ds \tag{70}$$

for the wave diffraction, and

$$q_R = \iint_{S_i} \frac{\partial\phi_3}{\partial z} ds \tag{71}$$

for the wave radiation.

Then, the wave loads on the OWC-WEC are given by:

$$f = \int_{S_B} pndS \tag{72}$$

$$M_y = \int_{S_B} p[(z - z_0)n_x - (x - x_0)n_z]dS \tag{73}$$

in which $n = (n_x, n_y, n_z)$ is the unit normal vector on the body surface, (x_0, z_0) is the rotational center, $f = (f_x, f_y, f_z)$, and p can be calculated from the linearized Bernoulli's equation as

$$p = -i\omega\rho\phi \tag{74}$$

The wave loads on the beam shown in Figure 1 can be obtained if S_B is replaced with the surface chamber shell in Equations (72) and (73).

3. Results and Discussions

3.1. Convergence and Validation

The convergence of the results with respect to the truncation number M in Equations (63)–(66) is firstly tested. The water depth h, gravitational acceleration g, and water density ρ are used as the base of non-dimensionalization in the following sections. In the first case, the parameters are set as $R_1/h = 0.5$, $R_2/h = 1.0$, $R_3/h = 1.50$, $d/h = 0.5$, and $kh = 1.0$. Figure 3 shows the obtained non-dimensional value of added mass B, damping coefficient C, and volume flux Q_D with different M. It can be seen that the numerical convergence can be obtained as $M \geq 20$. Similar convergence can also be realized for other cases with the same value of M.

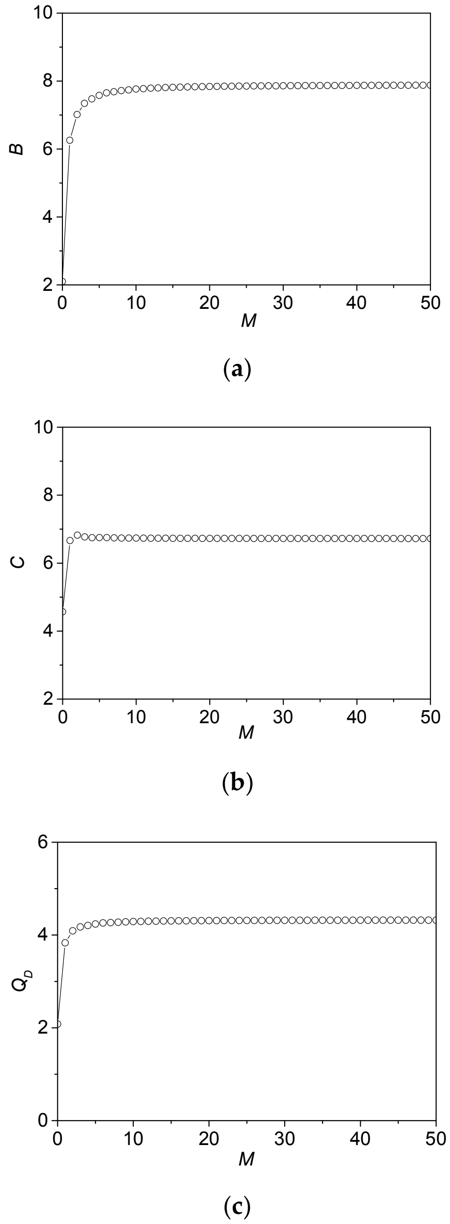

Figure 3. Convergence study with respect to parameter M, for (**a**) B, (**b**) C, and (**c**) Q_D.

Then, the validation of the present solution is examined. A higher-order BEM (boundary element method) [24] was applied to solve the diffraction problem with the same parameters as above. The rotation center is fixed at the bottom of the cylinder. Figure 4 shows the comparisons of wave forces in

x and z directions and moment about axis y obtained by the present method and BEM, respectively. From these comparisons, the numerical results given by two methods are in good agreement, which verifies the accuracy of the present analytical model.

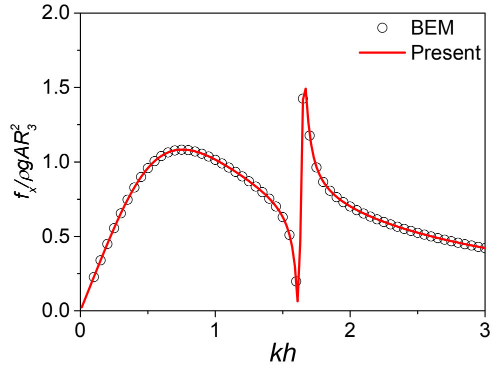

(**a**)

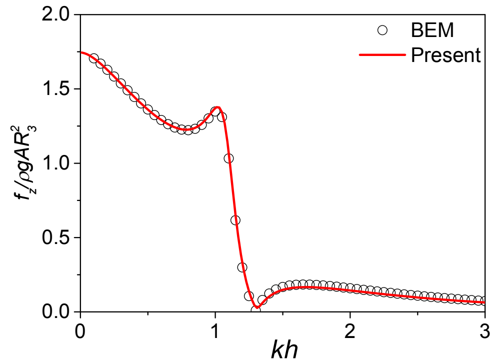

(**b**)

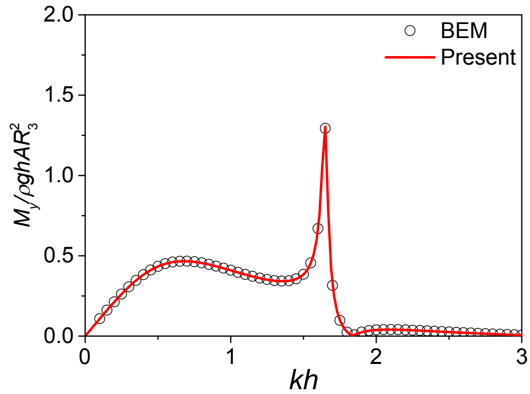

(**c**)

Figure 4. Comparison of hydrodynamic force amplitudes by the present model and the BEM: (**a**) wave force in x direction, (**b**) wave force in z direction, and (**c**) wave moment about axis y.

3.2. Determination of Turbine Rotate Speed

Effect of turbine rotate speed on the conversion efficiency is studied firstly. Martins-Rivas and Mei [18] simulated one OWC-WEC property in Pico Island, Azores, Portugal with N = 2000 r.p.m., K = 0.45 (for one turbine). As a preliminary study, the same sea depth and power take-off system were selected to simulate the present OWC-WEC. Figure 5 shows the efficiency distribution of the OWC-WEC, with different turbine rotate speeds N = 100 (r.m.p), N = 200 (r.m.p), N = 500 (r.m.p), N = 1000 (r.m.p), and N = 2000 (r.m.p). The remaining geometrical parameters are kept as R_1/h = 0.15, R_2/h = 0.50, R_3/h = 0.51, d/h = 0.2, K = 0.45, $V_0 = \pi R_2^2 h$ A/h = 0.1, and h = 10 m. It is found that there is one optimal conversion frequency for different turbine rotation speeds. Additionally, the optimal frequency shifts towards a lower frequency with the decrease of the turbine rotate speed. It is clear that the case of N = 200 (r.m.p) is consistent with the results obtained in Martins-Rivas and Mei's model. This is the result of the difference between the present and Martins-Rivas and Mei's models. Additionally, based on the semi-empirical Pierson-Moscowitz (P-M) energy density spectrum in 10 m sea depth, the wave frequency is in range of $1 \leq kh \leq 4$. Hence, the case of N = 200 (r.m.p) can be used to simulate the wave energy conversion in the present OWC-WEC.

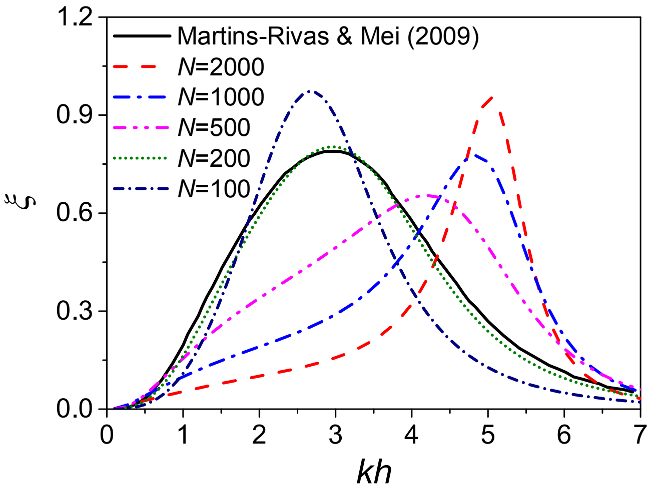

Figure 5. Distribution of hydrodynamic efficiency for different turbine rotational speed N on the efficiency ξ.

3.3. Wave Motion Inside the OWC Chamber

To study the wave phenomena inside the OWC chamber, an example is considered with the parameters of R_1/h = 0.15, R_2/h = 0.35, R_3/h = 0.4, d/h = 0.2, K = 0.45, N = 200 r.p.m, $V_0 = \pi R_2^2 h$, A/h = 0.1, and h = 10 m. The incident wave propagates in x-direction. Figure 6 shows the variation of the wave surface amplitude at two points $U_1(-0.20, 0.0)$ and $U_2(-0.30, 0.0)$ inside the chamber versus the dimensionless wave number kh. The vertical coordinate is normalized by the incident wave amplitude A. From the figure, it can be seen that both surface amplitudes at different positions vary in a similar trend with the wave frequency. In the low frequency region ($kh < 1.5$), the dimensionless surface amplitudes inside the chamber are near to 1, which is due to the fact that the chamber size is much smaller than the wave length, and the relating wave effects can be ignored. Then, three peaks occur at kh = 2.83, kh = 4.68, and kh = 8.15 with the increase of the wave frequency. W1, W2, and W3 are used to denote these three situations for convenience. It is also noticed that, compared with condition W1, the dimensionless surface amplitudes at the other two conditions show sharper peaks with singular feature.

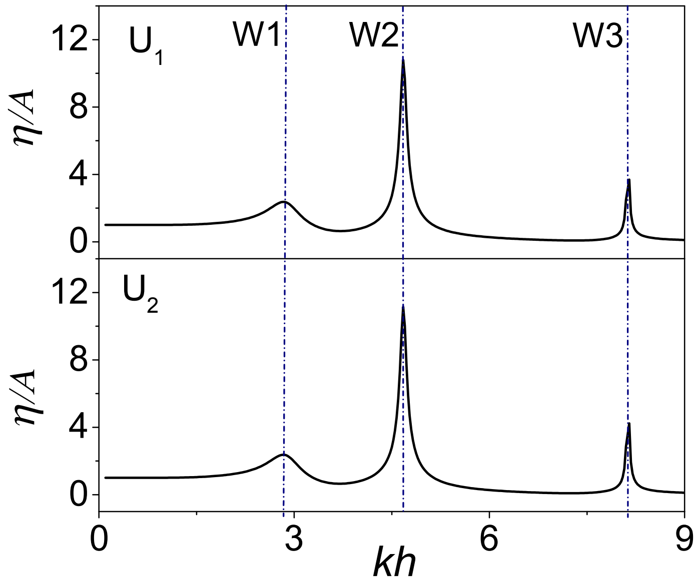

Figure 6. Variations of dimensionless surface amplitudes at two positions with *kh*.

Contours of surface oscillation amplitude inside the chamber are plotted in Figure 7 at situations W1, W2, and W3, respectively. Note that all amplitudes are normalized by the incident wave height A. From Figure 7, it can be seen that the wave amplitudes of the free surface are almost the same with each other at W1, which leads to a piston-type water oscillation in the chamber. However, the distributions of the free surface amplitudes at W2 and W3 are nearly symmetrical about $x = 0$ or $y = 0$. The phenomena in Figure 7b,c are in sloshing modes occurring at circumferential direction with order $m = 1$ and $m = 2$ in Equation (43), respectively.

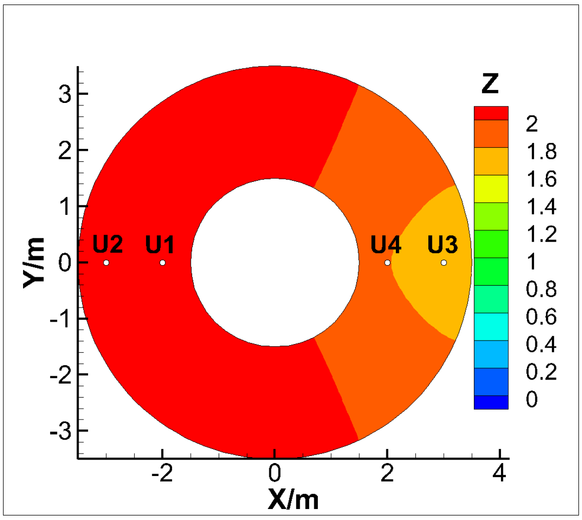

(**a**)

Figure 7. *Cont.*

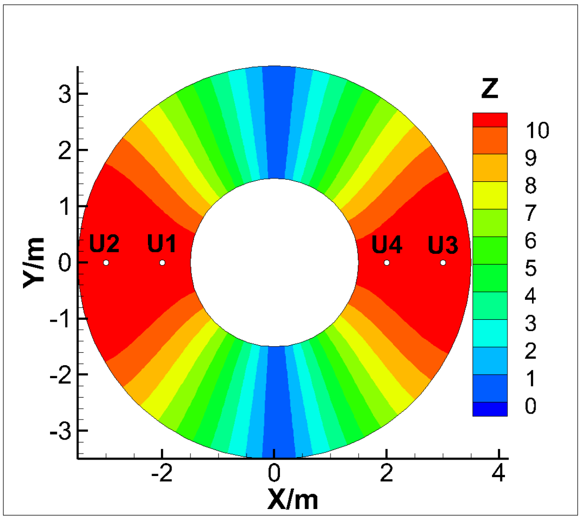

(**b**)

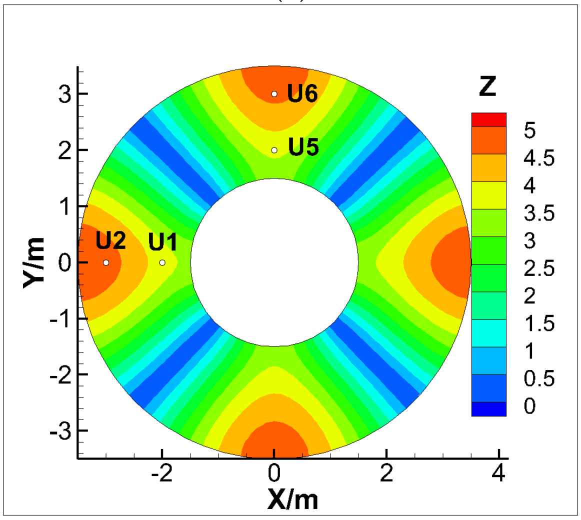

(**c**)

Figure 7. Contours of surface amplitudes in the chamber at (**a**) W1, (**b**) W2, and (**c**) W3 conditions.

To further analyze water motion inside the chamber, another four points $U_3(0.3,0)$, $U_4(0.2,0)$, $U_5(0,0.2)$, and $U_6(0,0.3)$ are considered as shown in Figure 7. Time series of the water elevations at these points are shown in Figure 8. From Figure 8a, it can be seen that the wave elevations at these four points in the chamber are always in phase and with the similar amplitude, as a feature of the piston-type oscillation. It further proves that the water inside the chamber at condition W1 oscillates as a piston, which can compress and expand the chamber air effectively. Strictly speaking, the wave amplitudes at these positions are not exactly same. This is due to the fact that a small-amplitude sloshing also occurs in the chamber at the same time, even though the piston motion is absolutely dominant at W1. For cases of W2 and W3, the free surface motions in the chamber are either centrosymmetric or antisymmetric about the plane $x = 0$ in Figure 8b,c. This means that, except for W1, there is no evident variation of the total air volume in the chamber. Figure 9 presents the distribution of power extraction efficiency ξ with dimensionless wave number kh. It can be seen that the extraction efficiency ξ reaches the peak at $kh = 2.83$, which just coincides with condition W1, i.e., the piston-type mode. Hence, it is the piston-type mode that makes the main contribution to the wave energy conversion.

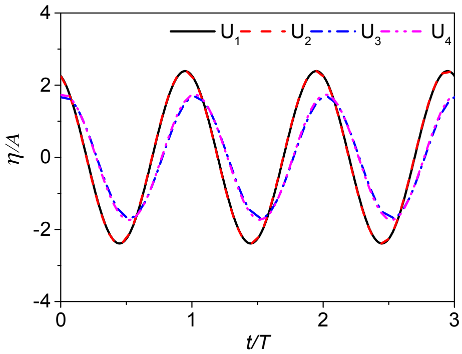

(**a**)

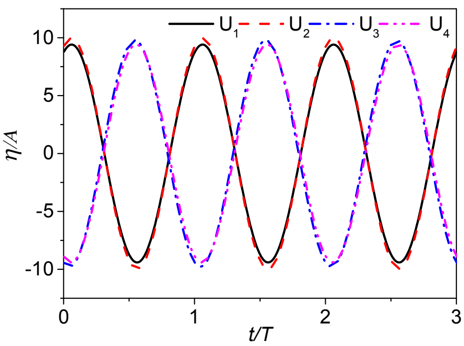

(**b**)

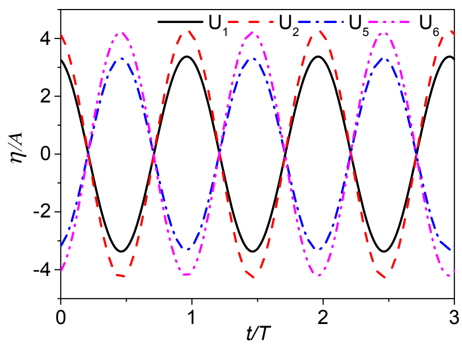

(**c**)

Figure 8. Time series of the free-surface elevation at test positions in the chamber at conditions (**a**) W1, (**b**) W2, and (**c**) W3.

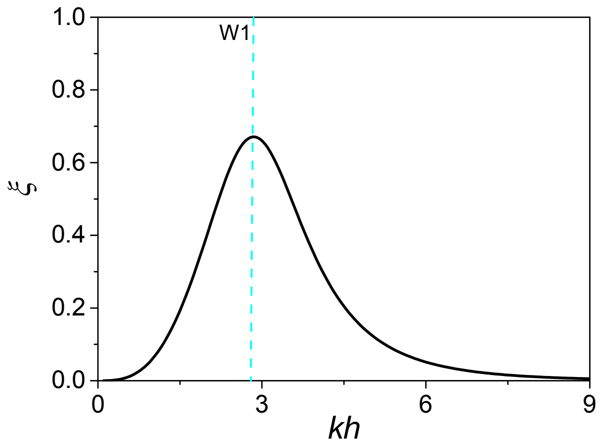

Figure 9. Distribution of extraction efficiency ξ with kh.

3.4. Effects of Geometry Parameters on Wave Loads and Extraction Efficiency

Both survivability and efficiency are important factors for a WEC. The effects of the OWC geometrical parameters on them are investigated in this section, which can be used as guidance for OWC optimization. To be specific, the chamber draft d, chamber breadth $b = R_2 - R_1$, and thickness of the chamber wall $d_{wall} = R_3 - R_2$ are taken into account. As the preliminary study, the main parameters are selected based on engineering practice to be with $D/h = 0.3$, $K = 0.45$, $N = 200$ r.p.m, $V_0 = \pi R_2^2 D$, $A/h = 0.1$, and $h = 10$ m.

Lateral wave force and bending moment are critical parameters for survivability and reliability in ocean engineering. Figure 10a,b shows the wave force f_x and bending moment M_y about sea bed on the whole OWC device with four chamber drafts, i.e., $d/h = 0.10$, $d/h = 0.20$, $d/h = 0.30$, and $d/h = 0.40$. The chamber breadth $b/h = 0.2$ and chamber wall thickness $d_{wall}/h = 0.05$ are fixed. Figure 10c shows the wave force $f_{x\text{beam}}$ of the chamber shell, and Figure 10d shows the chamber shell moment $M_{y\text{beam}}$ about the connection beam between the cylinder and the chamber. The beam is assumed above the water surface D/h = 0.30. In Figure 10a,b, two resonant peaks can be found within the considered range of $0 \leq kh \leq 6$ for both the wave force and moment. It is the first peak being of engineering interest. From the figure, it can be seen that as d/h change from 0.10 to 0.40, the first peaks of both the wave force f_x and moment M_y increase greatly due to the increase of the wet surface acting on the OWC-WEC. Hence, lower chamber draft is preferred to decrease the wave loads. In the high frequency domain, another resonant peak occurs. In Figure 10a, for the case of $d/h = 0.2$, the second peak occurs at $kh = 4.68$, which is exactly corresponding to condition W2 as shown in Figure 6. At $kh = 4.68$, the wave length $L/h = 0.67$, which is close to the chamber inner diameter $2R_2 = 0.70$. The incident waves are captured in $m = 1$ mode. Therefore, it can be concluded that the resonant sloshing mode at order $m = 1$ in Equation (43) induces an extreme wave load on the device at the second peak. The potential theory without considering the fluid viscidity leads to an over-prediction of the wave force at resonance. However, in real fluids, the wave loads at the W2 sloshing mode cannot be so large due to the viscous dissipation. Such peak wave force acting on the OWC-WEC increases sharply with the chamber draught. Additionally, the resonant sloshing frequency shifts towards a lower frequency. In other words, the sloshing resonance becomes much stronger with the increase of the chamber draught [16]. In Figure 10c,d, the beam force $f_{x\text{beam}}$ and bending moment $M_{y\text{beam}}$ vary with the same trend in Figure 10a,b. Compared with f_x and M_y, wave loads of the beam at the first peak decrease slightly. However, the resonant response at $m = 1$ mode is much higher than that in Figure 10a,b. Hence, in present OWC-WEC, lower chamber draught leads to higher survivability.

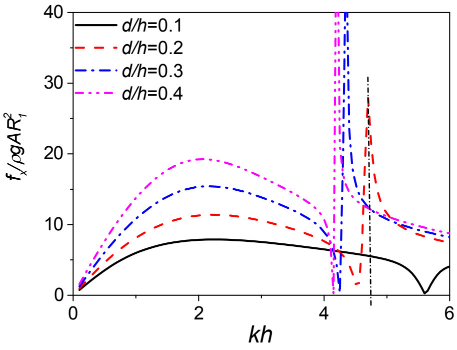

(**a**)

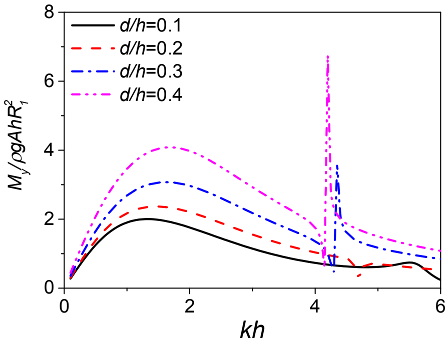

(**b**)

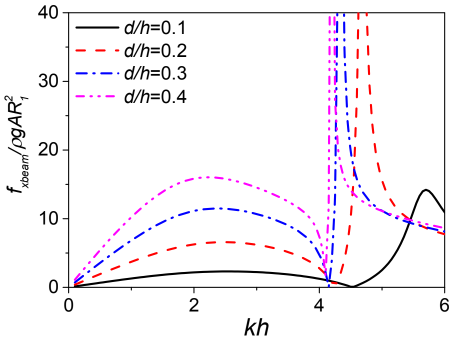

(**c**)

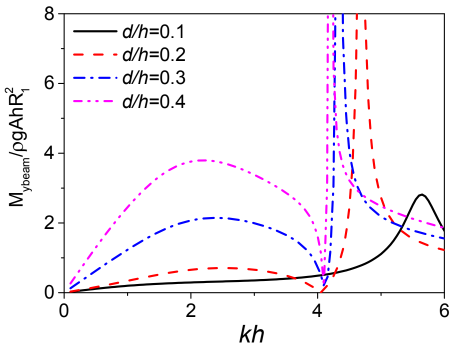

(**d**)

Figure 10. Effect of chamber draft on the hydrodynamic loads for d/h = 0.10, d/h = 0.20, d/h = 0.30, and d/h = 0.40. (**a**) Wave force f_x, (**b**) wave moment M_y, (**c**) wave force $f_{x\text{beam}}$, and (**d**) wave moment $M_{y\text{beam}}$.

Further, the effects of the chamber draught on power extraction efficiency are presented in Figure 11. A dash line at $\xi = 0.3$ is marked in the figure to depict the effective frequency bandwidth (i.e., the part for $\xi \geq 0.3$). The results indicate that the effective frequency bandwidth decreases largely with the reflected by a larger-draught. An explanation to such a phenomenon is that, in the high-frequency zone, the corresponding short waves with lower penetrability can be easily reflected by larger-draught chamber. From the figure, it also can be observed that the resonant frequency and maximal efficiency go up with the decrease of chamber draught. In other words, the proposed OWC device with a smaller chamber draft tends to possess a better capacity for wave energy conversion.

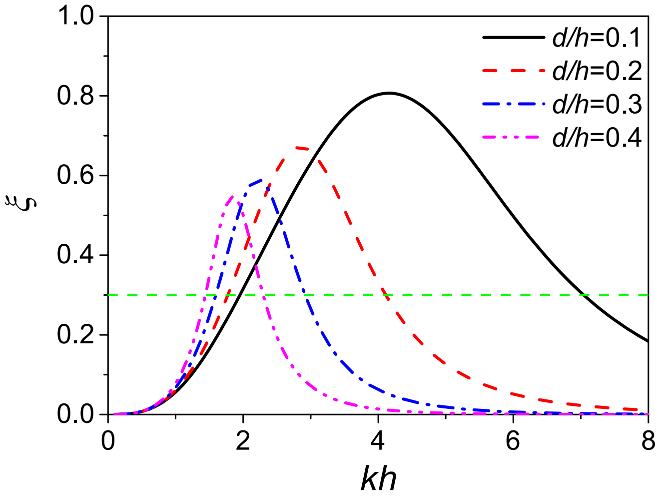

Figure 11. Effect of chamber draft on power extraction efficiency ξ for d/h = 0.10, d/h = 0.20, d/h = 0.30, and d/h = 0.40.

Figure 12 shows the effects of the chamber breadth on the hydrodynamic loads with four chamber breadths b/h = 0.10, b/h = 0.20, b/h = 0.30, and b/h = 0.40. The drafts and wall thickness of the chamber are set as constants d/h = 0.20 and d_{wall}/h = 0.05. In Figure 12a,b, there are also two resonant peaks shown in the considered range of kh for both the wave force and moment. As the chamber breadth increases, the wave moment M_y decreases greatly at the first resonant frequency. However, the wave force f_x on the device increases with the chamber breadth due to the increase of the chamber wall surface in domain Ω_1 leading to a larger wave force. In the high frequency domain, as b/h increases, the second resonant peak shifts towards a lower frequency and increases its magnitude slightly. For wider chamber breadth, the resonance of the sloshing model at order m = 1 occurs at the longer wave area. Figure 12c,d shows the wave loads of the connection beam with different chamber breadth. It also can be seen that the beam force $f_{x\text{beam}}$ and bending moment $M_{y\text{beam}}$ at the m = 1 mode are exceptionally high. Additionally, compared with f_x and M_y, the frequency bandwidth in W1 sloshing mode in Figure 12c,d increases with the chamber breadth; this is especially apparent for the bending moment $M_{y\text{beam}}$. Hence, for wider chamber breadth, the bending moment of the whole OWC-WEC decreases, even though the resonant loads of the connection beam increase greatly. Figure 13 shows the power extraction efficiency with different chamber breadths. It can be seen that the effective frequency bandwidth increases sharply with the chamber breadth for capturing longer waves. The reason for this is that the inertia of the water column in the chamber increases with chamber width. Thus, long wave energy captured can make a greater contribution to the piston-type oscillation in the chamber. It is also found that the resonant frequency decreases rapidly with chamber breadth. In other words, the proposed OWC with a wider chamber tends to possess better efficiency.

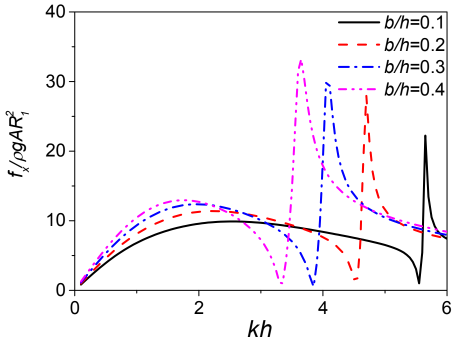

(**a**)

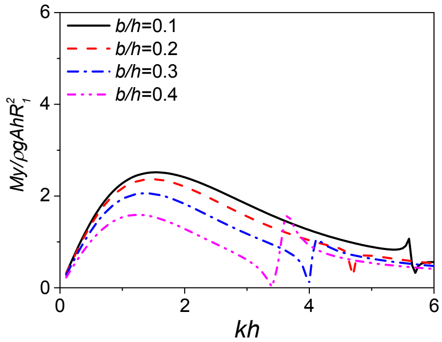

(**b**)

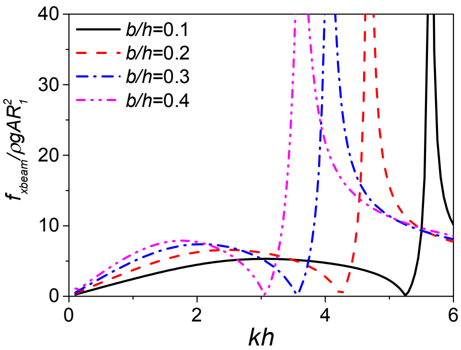

(**c**)

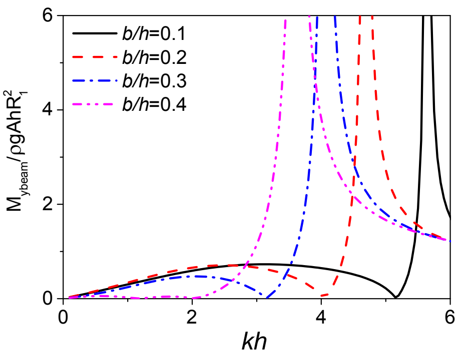

(**d**)

Figure 12. Effect of the chamber breadth on the wave loads for *b*/*h* = 0.10, *b*/*h* = 0.20, *b*/*h* = 0.30, and *b*/*h* = 0.40: (**a**) wave force f_x, (**b**) wave moment M_y, (**c**) wave force $f_{x\text{beam}}$, and (**d**) wave moment $M_{y\text{beam}}$.

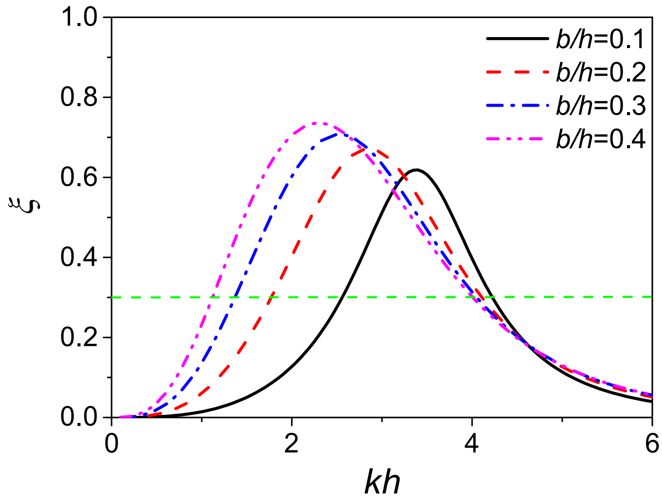

Figure 13. Effect of the chamber breadth on the energy extraction efficiency for b/h = 0.10, b/h = 0.20, b/h = 0.30, and b/h = 0.40.

Finally, the effects of the chamber wall thickness on the hydrodynamic loads and extraction efficiency are presented in Figures 14 and 15, respectively. Four different chamber wall thicknesses, i.e., $d_{wall}/h = 0.01$, $d_{wall}/h = 0.05$, $d_{wall}/h = 0.10$, and $d_{wall}/h = 0.15$, are considered. The other parameters are set as constant $d/h = b/h = 0.20$. It can be seen that the chamber wall thickness has little impact on the second resonant frequency, which is mainly decided by the chamber breadth. With the increase of the chamber wall thickness, at the first resonant peak, the wave force f_x increases, but the bending moment M_y decreases. An explanation to the latter is that, while increasing the chamber wall thickness, the wet surface of the proposed device in domain Ω_2 increases, which can reduce the bending moment M_y about the sea bed. Figure 15 shows the variation of extraction efficiency with four different thicknesses of the chamber wall. The results indicate that the extraction efficiency ξ and effective frequency bandwidth decrease as the wall thickness grows. However, compared with the results shown in Figures 11 and 13, the effect of the wall thickness on the resonant frequency is weaker. Therefore, for engineering considerations, the chamber wall thickness can be designed mainly according to extreme environmental loads and material strength.

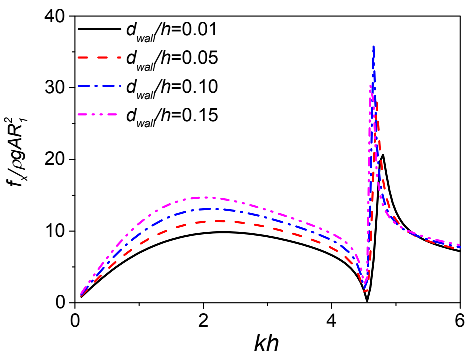

(**a**)

Figure 14. *Cont.*

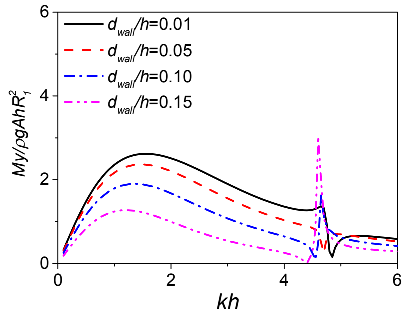

(**b**)

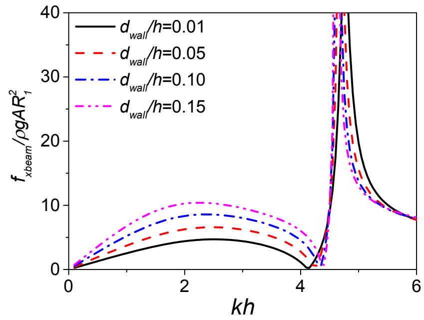

(**c**)

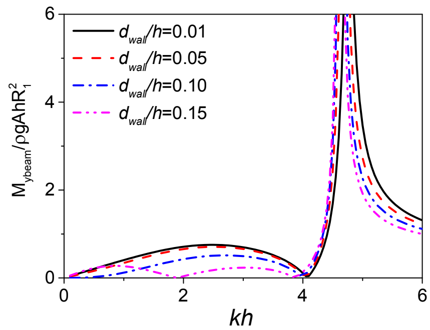

(**d**)

Figure 14. Effect of chamber wall thickness on the wave loads, for d_{wall}/h = 0.01, d_{wall}/h = 0.05, d_{wall}/h = 0.10, and d_{wall}/h = 0.15: (**a**) wave force f_x, (**b**) wave moment M_y, (**c**) wave force $f_{x\text{beam}}$, and (**d**) wave moment $M_{y\text{beam}}$.

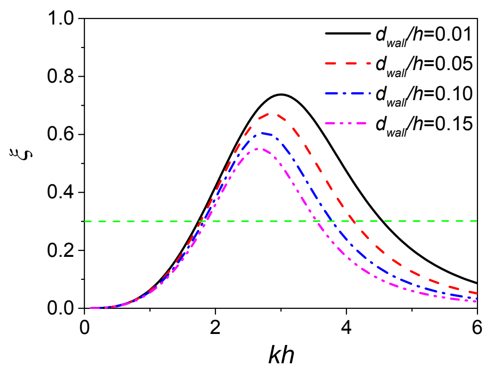

Figure 15. Effect of the chamber wall thickness on the energy conversion efficiency, for d_{wall}/h = 0.01, d_{wall}/h = 0.05, d_{wall}/h = 0.10, and d_{wall}/h = 0.15.

4. Conclusions

This research has provided an easy-to-deploy OWC-WEC design with good performance. This OWC-WEC is featured with an excellent adaption to offshore sites with multiple wave directions. The overall costs are expected to be reduced when a large-scale deployment is achieved. The structure has a mushroom appearance, which can be considered as an upside down cylindrical bucket supported by a column fixed on the seabed. A concentric cylindrical chamber is formed. The energy is transformed from the wave to the air by an oscillating water column moving up and down in the chamber. As the bidirectional airflow flows through the orifice on the top of the chamber, the turbine drives an electricity generator. Compared with the existing shoreline OWC devices, this wave energy device is not restricted by the wave directions and coastline geography conditions.

Then, analytical solutions are derived based on the linear potential-flow theory to investigate hydrodynamic properties of the wave energy converter. The wave motion inside the chamber and the effect of geometry parameters on the hydrodynamic loads and extraction efficiency are investigated. Three typical free-surface oscillation modes in the chambers are found and analyzed. The piston-type mode, which can compress the chamber air efficiently, makes the largest contribution to the energy conversion efficiency. Further, it is found that, as the chamber draft decreases, the resonant frequency and peak efficiency increase apparently, and the wave loads on the whole OWC-WEC also decrease greatly. Additionally, for the design of the connection beam, the wave loads at $m = 1$ mode should be considered, especially the OWC-WEC with wider chamber breadth. For wider effective frequency bandwidth, the OWC shell can be selected with lower draft and wider chamber breadth. Compared with the chamber draft and breadth, the chamber wall thickness has a relatively small impact on the wave energy conversion, which can be designed by environmental loads and material strength in engineering. In the next stage, a series of model experiments (e.g., similar to those in Viviano et al. [25]) will be carried out for further investigation based on the present analytical solutions.

Acknowledgments: This study is supported by the National Science Foundation of China (Grant Nos. 51679036, 51490672, and 51709038) and the Royal Academy of Engineering under the UK-China Industry Academia Partnership Programme (Grant No. UK-CIAPP\73).

Author Contributions: Yu Zhou, Chongwei Zhang and Dezhi Ning drafted the work, made substantial contributions to the design of the work, gave the final approval of the version to be published, and agreed to be accountable for all aspects of the work in ensuring that questions related to the accuracy or integrity of any part of the work are appropriately investigated and resolved.

Conflicts of Interest: The authors declare no conflict of interest.

References

1. Falcão, A.F.O. Wave energy utilization: A review of the technologies. *Renew. Sust. Energy Rev.* **2010**, *14*, 899–918. [CrossRef]
2. Borthwick, A.G. Marine Renewable Energy Seascape. *Engineering* **2016**, *2*, 69–78. [CrossRef]
3. Henderson, R. Design, simulation, and testing of a novel hydraulic power take-off system for the Pelamis wave energy converter. *Renew. Energy* **2006**, *31*, 271–283. [CrossRef]
4. He, F.; Huang, Z.; Law, W.K. An experimental study of a floating breakwater with asymmetric pneumatic chambers for wave energy extraction. *Appl. Energy* **2013**, *106*, 222–231. [CrossRef]
5. Monk, K.; Zou, Q.; Conley, D. An approximate solution for the wave energy shadow in the lee of an array of overtopping type wave energy converters. *Coast. Eng.* **2013**, *73*, 115–132. [CrossRef]
6. Falcão, A.F.O.; Justino, P.A.P. OWC wave energy devices with air flow control. *Ocean Eng.* **1999**, *26*, 1275–1295. [CrossRef]
7. Heath, T.V. A review of oscillating water columns. *Philos. Trans.* **2012**, *370*, 235–245. [CrossRef] [PubMed]
8. Falcão, A.F.O.; Henriques, J.C.C. Oscillating-water-column wave energy converters and air turbines: A review. *Renew. Energy* **2016**, *85*, 1391–1424. [CrossRef]
9. Masuda, Y.; Mccormick, M.E. Experiences in pneumatic wave energy conversion in Japan. In *Utilization of Ocean Waves—Wave to Energy Conversion*; ASCE Library: Reston, VA, USA, 2015; pp. 1–33.

10. Zhang, D.; Li, W.; Lin, Y. Wave energy in China: Current status and perspectives. *Renew. Energy* **2009**, *34*, 2089–2092. [CrossRef]
11. Boccotti, P. Comparison between a U-OWC and a conventional OWC. *Ocean Eng.* **2007**, *34*, 799–805. [CrossRef]
12. Naty, S.; Viviano, A.; Foti, E. Wave Energy Exploitation System Integrated in the Coastal Structure of a Mediterranean Port. *Sustainability* **2016**, *8*, 12. [CrossRef]
13. Bingham, H.B.; Ducasse, D.; Nielsen, K.; Read, R. Hydrodynamic analysis of oscillating water column wave energy devices. *J. Ocean Eng. Mar. Energy* **2015**, *1*, 405–419. [CrossRef]
14. Ogata, T.; Washio, Y.; Osawa, H.; Tsuritani, Y.; Yamashita, S.; Nagata, Y. The Open Sea Tests of the Offshore Floating Type Wave Power Device "Mighty Whale": Performance of the Prototype. *Oceans* **2002**, *4*, 1860–1866.
15. Alcorn, R.; Blavette, A.; Healy, M.; Lewis, A. FP7 EU funded CORES wave energy project: A coordinators' perspective on the Galway bay sea trials. *Underw. Technol.* **2016**, *32*, 51–59. [CrossRef]
16. Garrett, C.J.R. Bottomless harbours. *J. Fluid Mech.* **2006**, *43*, 433–449. [CrossRef]
17. Sarmento, A.J.N.A.; Falcão, A.F.O. Wave generation by an oscillating surface-pressure and its application in wave-energy extraction. *J. Fluid Mech.* **1985**, *150*, 467–485. [CrossRef]
18. Martins-Rivas, H.; Mei, C.C. Wave power extraction from an oscillating water column at the tip of a breakwater. *J. Fluid Mech.* **2009**, *626*, 395–414. [CrossRef]
19. Martins-Rivas, H.; Mei, C.C. Wave power extraction from an oscillating water column along a straight coast. *Ocean Eng.* **2009**, *36*, 426–433. [CrossRef]
20. Zhu, S.P.; Mitchell, L. Diffraction of ocean waves around a hollow cylindrical shell structure. *Wave Motion* **2009**, *46*, 78–88. [CrossRef]
21. Konispoliatis, D.N.; Mazarakos, T.P.; Mavrakos, S.A. Hydrodynamic analysis of three–unit arrays of floating annular oscillating–water–column wave energy converters. *Appl. Ocean Res.* **2016**, *61*, 42–64. [CrossRef]
22. Falcão, A.F.O. Wave-power absorption by a periodic linear array of oscillating water columns. *Ocean Eng.* **2002**, *29*, 1163–1186. [CrossRef]
23. Evans, D.V. Wave-power absorption by systems of oscillating surface pressure distributions. *J. Fluid Mech.* **1982**, *114*, 481–499. [CrossRef]
24. Teng, B.; Taylor, R.E. New higher-order boundary element methods for wave diffraction/radiation. *Appl. Ocean Res.* **1995**, *17*, 71–77. [CrossRef]
25. Viviano, A.; Naty, S.; Foti, E.; Bruce, T.; Allsop, W.; Vicinanza, D. Large-scale experiments on the behaviour of a generalised Oscillating Water Column under random waves. *Renew. Energy* **2016**, *99*, 875–887. [CrossRef]